Faraday Discussions
Cite this: *Faraday Discuss.*, 2023, **243**, 126

PAPER

View Article Online
View Journal | View Issue

Switching on/off molybdenum nitride catalytic activity in ammonia synthesis through modulating metal–support interaction†

Amanda Sfeir,[a] Camila A. Teles,[a] Maya Marinova,[b] Hérve Vezin,[c] Jean-Philippe Dacquin,[a] Axel Löfberg,[a] Said Laassiri*[d] and Sébastien Royer *[a]

Received 15th November 2022, Accepted 6th December 2022
DOI: 10.1039/d2fd00154c

Modulating the interaction between Mo nanoparticles and their support is an elegant approach to finely tune the structural, physico-chemical, redox and electronic properties of the active site. In this work, a series of molybdenum nitride catalysts supported on TiO_2, and SBA-15 has been prepared and fully characterized. The results of characterization confirmed the high dispersion of Mo and the formation of small molybdenum nanoparticles in both the 10-Mo-N/SBA-15 and 10-Mo-N/TiO_2 catalysts. In this context, we have shown that the catalytic activity of Mo species was strongly impacted by the nature of the catalytic support. Amongst the studied supports, SBA-15 was found to be the most appropriate for Mo dispersion. In comparison, when supported on a reducible oxide (TiO_2), Mo species showed poor catalytic activity in both ammonia synthesis and decomposition and were prone to quick deactivation in the ammonia synthesis reaction. Evidence of charge transfer from the reducible support to the active phase, indicative of possible SMSI behaviour, has been observed by XPS and EPR. Differences in the oxidation states, redox behaviours, and electronic properties have been further studied by means of EPR, H_2-TPR and H_2-TPD.

1 Introduction

Possessing high catalytic activity and selectivity, molybdenum-based materials are considered key catalysts in multiple reactions of high industrial and academic

[a]*Univ. Lille, CNRS, Centrale Lille, Univ. Artois, UMR 8181 – UCCS – Unité de Catalyse et Chimie du Solide, F-59000 Lille, France. E-mail: sebastien.royer@univ-lille.fr*
[b]*Université de Lille, CNRS, INRA, Centrale Lille, Université Artois, FR 2638 – IMEC – Institut Michel-Eugène Chevreul, 59000 Lille, France*
[c]*Laboratoire de Spectroscopie pour Les Interactions La Réactivité et L'Environnement Université de Lille, UMR CNRS 8516-LASIRE, 59000 Lille, France*
[d]*Chemical & Biochemical Sciences, Green Process Engineering (CBS), Mohamed VI Polytechnic University, UM6P, 43150, Benguerir, Morocco. E-mail: said.laassiri@um6p.ma*
† Electronic supplementary information (ESI) available. See DOI: https://doi.org/10.1039/d2fd00154c

interest including hydrodesulfurization (HDS),[1,2] oxidative desulfurization,[3,4] CO_2 conversion[5,6] and ammonia synthesis.[7] The versatility of Mo arises from (i) its redox properties as it possesses different oxidation states and (ii) its ability, upon reaction with appropriate precursors, to form a range of carbide,[8,9] nitride,[10,11] phosphide[12,13] and sulphide[14,15] materials with different crystalline structures. The high "malleability" of Mo chemical composition allows the careful tuning of its electronic properties, textural and structural properties, surface terminations, site occupancies, defect concentration, and surface properties, which in many cases are determining parameters controlling the catalytic activity and selectivity.

Over the years, molybdenum related phases have driven much interest in ammonia synthesis due to the importance of the latter in the production of reactive nitrogen for the fertilizer industry. A wide range of Mo-based catalysts has been studied for ammonia generation including Mo carbides and supported Mo carbides (β-Mo_2C, Mo_2C/C support, Mo_2C/CeO_2),[16–19] nitrides and supported nitrides (γ-Mo_2N, β-Mo_2N, δ-MoN, δ-MoN_x/ZSM-5),[7,16,20] bimetallic Mo nitrides and carbides (Co_3Mo_3N, Ni_2Mo_3N, Co_3Mo_3C), *etc.*[21–24] The application of Mo-based materials was not only restricted to heterogeneous catalytic ammonia synthesis but was also extended to alternative processes such as chemical looping,[25] electro-chemistry,[26] and photocatalysis.[27,28] The interest in molybdenum activity can trace its original roots back to the earlier work of Volpe and Boudart[20] and Oyama,[29] reporting high catalytic activity of Mo_2N for ammonia synthesis, at atmospheric pressure and 400 °C.[29] However, throughout the years, the chemical composition, facet surface description, and structure of Mo have been reported to affect the catalytic activity and reaction mechanism. For instance, differences in the catalytic activity of β-Mo_2N and δ-MoN were reported with the latter being less active at 400 °C and ambient pressure.[30] Furthermore, the degree of Mo nitridation was reported to influence greatly the nature of the rate determining step when metallic and nitride phases are compared.[31] These differences have also been reported in the case of molybdenum carbides crystallizing in different structures. The ammonia synthesis activity of β-Mo_2C (5.8 $mmol_{NH_3}\ g_{cat}^{-1}\ h^{-1}$) was found to be higher than that of α-MoC (2.3 $mmol_{NH_3}\ g_{cat}^{-1}\ h^{-1}$) at 400 °C and 1.0 MPa.[32] These results were explained based on changes observed in the adsorption–desorption properties of nitrogen, hydrogen and ammonia, being dependant on the nature of the crystalline structure of molybdenum carbide.[32] Considering the structure-sensitive nature of ammonia synthesis using molybdenum, it is of paramount importance to devise new strategies to improve the catalytic activity and stability of Mo by the careful tuning of its local structure and chemical composition.

A further consideration, that is not largely envisioned when designing novel Mo-based systems, is the importance of metal–support interaction in modulating the activity for a given reaction. Such interactions, referred to in the literature as strong metal–support interactions (SMSIs), have been studied extensively, particularly for noble metal-reducible oxides such as titania, ceria or iron oxide.[33] The classical SMSI is usually characterized by a migration of support-derived species over the metal surface leading to the encapsulation of the active phase which suppresses its ability to chemisorb small molecules and intermediates.[34] SMSI results in fundamental changes in the electronic and geometric nature of the active phase. In ammonia synthesis, where the reaction is governed by nitrogen adsorption and activation on the surface, it is of great interest and

importance to comprehend the role of metal–support interaction in engineering the electronic and geometric properties of Mo and as a consequence modulating its catalytic activity. To this end, Mo supported on mesoporous silica (SBA-15) and titanium oxide (TiO_2) has been successfully prepared by incipient wetness impregnation (IWI) and studied in the ammonia synthesis reaction and in ammonia decomposition. SBA-15 was studied as a non-reducible support presenting (i) high surface area; (ii) highly ordered and uniform mesopores; and (iii) good thermal stability. On the other hand, TiO_2 was studied as a reducible support capable of manifesting the SMSI effect. The effect of the support in altering the catalytic activity of molybdenum was evaluated in the ammonia synthesis reaction and in ammonia decomposition. SBA-15 was found to be the most appropriate support for molybdenum dispersion in both ammonia synthesis and ammonia decomposition. When supported on the reducible oxide TiO_2, molybdenum showed poor catalytic activity and was prone to quick deactivation especially in the ammonia synthesis reaction. The effect of the nature of the support on the physicochemical properties and catalytic activity of Mo species was investigated through an extensive characterization study.

2 Experimental section

2.1 Catalyst preparation

2.1.1 Chemicals. All chemicals needed for the preparation of supported molybdenum nitride catalysts and non-supported β-Mo_2N were used as purchased without further purification: tetraethylorthosilicate ($Si(OC_2H_5)_4$, TEOS, 98 wt%, Sigma-Aldrich), non-ionic triblock co-polymer Pluronic P123 (poly(ethylene glycol)-*block*-poly(propylene glycol)-*block*-poly(ethylene glycol), average MW ~5800, Sigma-Aldrich), ammonium *para*-heptamolybdate tetrahydrate ($(NH_4)_6Mo_7O_{24}\cdot 4H_2O$, 99 wt%, Alfa Aesar) and TiO_2 (Saint-Gobain NORPRO ST61120).

2.1.2 Supported Mo–N catalysts

2.1.2.1 10-Mo-N/SBA-15. SBA-15 was synthesized by a hydrothermal method, under acidic conditions as described elsewhere.[35]

The supported materials were synthesized by incipient wetness impregnation (IWI). The calculated weight of the Mo precursor $(NH_4)_6Mo_7O_{24}\cdot 4H_2O$ (Alfa Aesar) was dissolved in a volume corresponding to the pore volume of the respective support and then mixed. The mixture was aged for 5 days at 25 °C and then calcined at 400 °C (1.5 °C min^{-1}) for 5 h. The obtained Mo–O/SBA-15 underwent a pre-treatment step at 700 °C (5 °C min^{-1}) under a 75 vol% H_2/N_2 (BOC, 99.98%) (WHSV 18 000 mL g^{-1} h^{-1}) gas mixture at a total gas flow of 60 mL min^{-1} for 2 h in order to obtain the nitride form Mo–N/SBA-15.

2.1.2.2 10-Mo-N/TiO_2. Mo–N supported on TiO_2 was prepared by incipient wetness impregnation (IWI) as described for the preparation of 10-Mo-N/SBA-15.

2.1.2.3 β-Mo_2N preparation. Molybdenum oxide was prepared by the hydrothermal synthesis method. The Mo precursor (ammonium molybdate tetrahydrate, $(NH_4)_6Mo_7O_{24}\cdot 4H_2O$, Alfa Aesar) was dissolved in distilled water. The pH was adjusted to 1 by adding dropwise a 2 M solution of HNO_3. Thereafter, the solution was subjected to hydrothermal ageing at 180 °C in a Teflon autoclave for 12 h. After recovery by filtration, the solid was washed with water and dried at 60 °C overnight. The sample was then calcined at 300 °C (1.5 °C min^{-1}) for 5 h. α-MoO_3 underwent a pre-treatment step at 700 °C (5 °C min^{-1}) under a 75 vol%

H_2/N_2 (BOC, 99.98%) gas mixture at a total gas flow of 60 mL min^{-1} (WHSV 18 000 mL g^{-1} h^{-1}) for 2 h in order to obtain the nitride form β-Mo_2N.

N.B. Herein, the samples obtained after the calcination step are denoted as *X*-Mo-O/support. The catalysts obtained after the pre-treatment step are referred to as *X*-Mo-N/support, and the post-reaction samples are referred to as *X*-Mo-N-PR/support, where *X* is the wt% of α-MoO_3 ($X = 10$ wt%).

2.2 Catalyst characterization

2.2.1 Powder X-ray diffraction (PXRD). Wide angle PXRD patterns were collected using a Bruker X-ray AXS D8 Advance diffractometer in the Bragg–Brentano geometry configuration fitted with a LynxEye Super Speed detector. XRD patterns were recorded with Cu Kα radiation ($\lambda = 1.54184$ Å) at 40 kV and 30 mA. Patterns were recorded over a 2θ range of 10–80°, at a step size of 0.02° per step and a counting time of 0.5 s per step. Crystal phase identification was carried out by comparison with the ICDD database.

2.2.2 Small angle X-ray scattering (SAXS). Small angle X-ray scattering (SAXS) was performed on a Xeuss 2.0 (Xenocs) instrument operated under vacuum with a GeniX3D microsource ($\lambda = 1.54184$ Å) at 0.6 mA and 50 kV and a 2D Pilatus 3R 200K detector.

2.2.3 ICP-OES. The molybdenum content in the prepared materials was determined by ICP-OES analysis using a sequential scanning inductively coupled plasma with optical emission spectrometer (PerkinElmer Optima 2000 DV). The samples were previously dissolved in a diluted solution of HF–HCl and heated under microwave irradiation until complete dissolution.

2.2.4 Elemental analysis. Following the ammonia synthesis reaction, the nitrogen analysis in post-reaction catalysts was carried out using a Vario Cube elemental analyser.

2.2.5 Nitrogen physisorption. Textural properties were investigated using the adsorption/desorption isotherms of N_2 recorded at −196 °C on a Micromeritics Tristar II automated gas sorption system, operated with MicroActive software version 4.06. Prior to the analysis, the catalysts were outgassed under a dynamic vacuum at 300 °C for 3 h. The specific surface area, S_{BET}, was calculated from the linear part of the Brunauer–Emmett–Teller plot (10 points BET Method). The total pore volume (V_{pore}) was determined from the plateau of the adsorption branch at $P/P_0 = 0.97$. The pore size, D_{BJH}, was evaluated using the Barret–Joyner–Halenda method applied to the adsorption branch while the micropore volume (V_{micro}) was determined by the *t*-plot method.

2.2.6 X-ray photoelectron spectroscopy (XPS). XPS spectra were recorded on a Kratos Analytical AXIS Ultra DLD spectrometer employing monochromatic Al Kα X-ray radiation (1486.6 eV), with an electron analyser operating at a fixed pass energy of 20 eV. All binding energies (BEs) were referenced to the carbon signal corresponding to C–C bonding in the C 1s core level at 284.8 eV. A pre-treatment chamber was used in order to mimic the catalytic pre-treatment, prior to analysis, at 700 °C (5 °C min^{-1}) for 2 h under a 60 mL min^{-1} flow of 75 vol% H_2/N_2 (WHSV 18 000 mL g^{-1} h^{-1}).

2.2.7 Electron microscopy (TEM). Morphology analysis was performed using a TITAN Themis 300 S/TEM equipped with a high brightness Schottky field emission gun, a monochromator and a probe aberration corrector, allowing

energy and spatial resolution of about 150 meV and 70 pm, respectively. The microscope is equipped with several annular dark field detectors and a super-X detector system with four windowless silicon drift detectors for electron dispersive X-ray spectroscopy (EDS). The experiments were performed at 300 kV with a semi-convergence angle of about 20 mrad, probe size of the order of 500 pm and probe current between 60 and 100 pA. For high angle annular dark field (HAADF) imaging the *c* collection angles were between 50 and 200 mrad. EDS mapping was carried out in spectrum imaging mode with a dwell time per pixel of about 15 μs and continuous scanning of frames for a total acquisition time of about 15 to 20 minutes. The samples were deposited on 200 mesh lacey carbon, while the SBA-15 samples were frozen at −120 °C in distilled water and then cut to 70 nm with an ultramicrotome equipped with a 35° diamond knife (Leica UCT Ultracut). Cuts were then deposited on a 200 mesh lacey carbon grid for analysis.

2.2.8 Continuous-wave electron paramagnetic resonance measurement (CW EPR). CW EPR experiments were recorded at 9.5 GHz using a Bruker high temperature resonator at 700 °C. The experimental set up involved a modulation amplitude of 1 G and a microwave power of 5 mW. The kinetic experiments were realised under a gaseous mixture of 75 vol% H_2/N_2. The spectra were collected for 2 hours with a spectrum recorded every 40 s.

2.2.9 Redox properties. H_2-temperature programmed reduction (H_2-TPR) was conducted on an Autochem Chemisorption Instrument (Micromeritics) equipped with a TCD. Before analysis, the samples were pre-treated at 200 °C under a 50 mL min^{-1} flow of synthetic air (heating rate of 5 °C min^{-1}, 30 min). After cooling down to room temperature, the H_2-TPR was performed under a 50 mL min^{-1} flow of 5.0 vol% H_2 in Ar up to 1000 °C, with a heating rate of 5 °C min^{-1}.

2.2.10 Hydrogen chemical adsorption. H_2-temperature programmed desorption (H_2-TPD) was conducted on an Autochem Chemisorption Instrument (Micromeritics) equipped with a TCD. In a typical test, 0.5 g of Mo–O/support was added to the reactor and pre-treated under similar conditions to the pre-treatment reaction in order to obtain Mo–N/support (700 °C for 2 h under 75% H_2 in N_2). The reactor was then cooled under the same gas mixture to reach ambient temperature. Ar gas flow was used in order to purge the sample for 1 h followed by the adsorption of H_2 (5% H_2 in Ar) and then the gas was switched back to Ar for 1 h to remove all the physisorbed molecules of H_2. The H_2 desorption was measured by increasing the temperature (1 °C min^{-1}) until reaching 700 °C.

2.3 Catalytic activity

2.3.1 Ammonia synthesis. The reaction was performed at 400 °C and atmospheric pressure using a gas mixture of 75 vol% H_2/N_2 (BOC, 99.98%) at a total gas flow of 60 mL min^{-1}. 0.15–0.30 g (supported and bulk respectively) of material was placed in a quartz reactor tube and held centrally between two pieces of quartz wool in the heated zone of the furnace. The material was activated at 700 °C (5 °C min^{-1}) under 75 vol% H_2/N_2 (BOC, 99.98%) at 60 mL min^{-1} for 2 h (WHSV 18 000 mL g^{-1} h^{-1}) . After the activation step, the reactor was cooled down, and the reaction was performed at 400 °C.

The reactor effluent steam was flowed into a 200 mL H_2SO_4 solution (0.0018 M) and ammonia production was calculated from the decrease in conductivity. The catalytic activity was monitored as a function of reaction time.

2.3.2 Ammonia decomposition. In a typical test, 0.6 g of catalyst was placed in a quartz reactor under a 15 vol% NH_3/Ar (BOC, 99.98%) gas mixture at a total gas flow of 100 mL min^{-1}. The catalytic activity was measured between 250 and 700 °C at steps of 100 °C (30 min at each step) from 250 to 450 °C, and steps of 50 °C (30 min at each step) up to 700 °C. Ammonia conversion was determined using an FTIR analyser.

3 Results

3.1 Textural and structural properties

3.1.1 X-ray diffraction. Fig. 1 shows the PXRD patterns recorded in the wide-angle domain for α-MoO_3, β-Mo_2N, 10-Mo-O/SBA-15, 10-Mo-N-PR/SBA-15, 10-Mo-O/TiO_2 and 10-Mo-N-PR/TiO_2.

First the transformation of bulk molybdenum oxide α-MoO_3 into β-Mo_2N after the activation step was verified by PXRD (Fig. 1a). After the pre-treatment step, a single β-Mo_2N phase was formed. The diffractogram showed intense PXRD reflections indicating the formation of a well-crystallized material with all the peaks corresponding to the β-Mo_2N phase (PDF 25-1368).

PXRD diffractograms of 10-Mo-O/TiO_2 and 10-Mo-N-PR/TiO_2 are presented in Fig. 1b. For both materials only diffraction related to TiO_2 in the anatase phase

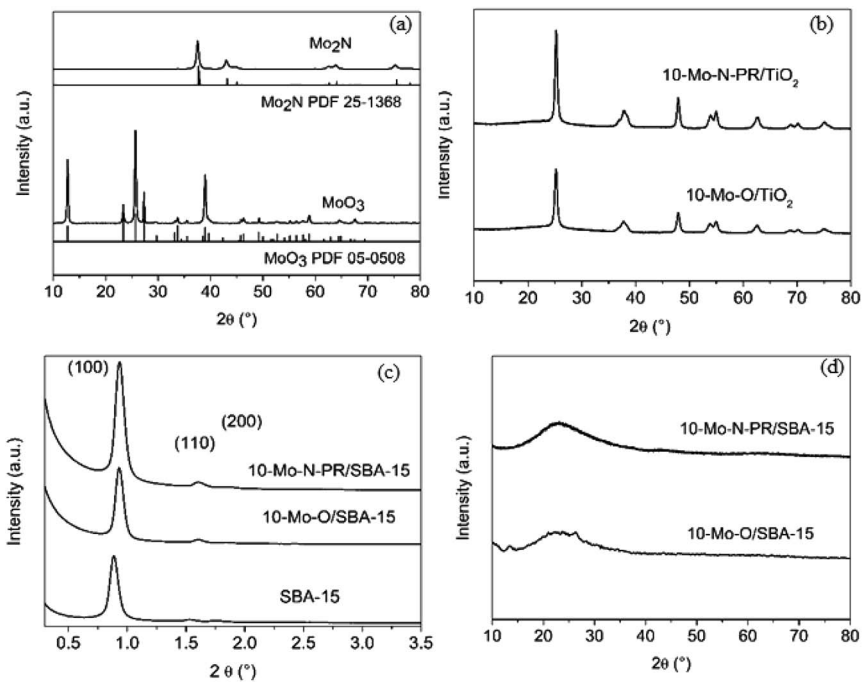

Fig. 1 XRD diffractograms of (a) unsupported α-MoO_3 and β-Mo_2N, (b) 10-Mo-O/TiO_2 and 10-Mo-N-PR/TiO_2, (c) SAXS diffractograms of 10-Mo-O/SBA-15 and 10-Mo-N-PR/SBA-15 and (d) wide angle domain diffractograms of 10-Mo-O/SBA-15 and 10-Mo-N-PR/SBA-15. *10-Mo-N-PR/TiO_2 and 10-Mo-N-PR/SBA-15 are post-ammonia synthesis reaction catalysts obtained after 1000 min in stream.

(PDF 78-2486) is observed. The absence of XRD reflections corresponding to the molybdenum oxide/nitride phase suggests that the crystallite size is small and molybdenum species are well dispersed on TiO_2.

SAXS patterns of the as-prepared siliceous support were collected before and after IWI impregnation and are presented in Fig. 1c. The calcined SBA-15 displays the three characteristic well-resolved diffraction peaks that can be associated with the (100), (110), and (200) planes of the *P6mm* hexagonal symmetry structure, reflecting the well-defined and uniform mesoporous structure of SBA-15. Upon Mo impregnation, the SAXS pattern of 10-Mo-O/SBA-15 showed that the support maintained its pore structure (Fig. 1c). However, an apparent shift of the reflection peaks to higher 2θ angle, from 0.88° to 0.93°, can also be observed, indicating a slight pore contraction upon Mo impregnation. No further changes were observed upon reaction, confirming the stability of the 10-Mo-N/SBA-15 catalyst under reaction conditions. The effectiveness of the dispersion of Mo oxides on the surface of SBA-15 was confirmed by PXRD in the wide-angle domain (Fig. 1d). The PXRD diffractogram was characterised by broad PXRD peaks of amorphous silica, and poorly defined reflection peaks related to the molybdenum oxide phase were observed, reflecting a well dispersed active phase. Surprisingly, upon reaction, no molybdenum nitride reflections were observed.

3.1.2 Nitrogen adsorption–desorption analysis. The textural properties of supported molybdenum oxide were investigated by means of N_2-physisorption. The results are summarized in Fig. 2, and Table 1.

The unsupported α-MoO_3 exhibited a type II isotherm (Fig. 2a) which is characteristic of non-porous materials and possessed a limited accessible surface area of $\sim$4 m^2 g^{-1}. The N_2 adsorption/desorption isotherm of 10-Mo-O/SBA-15 exhibited a type IV isotherm with an H1 hysteresis loop which is characteristic of ordered mesoporous materials. Additionally, a narrow pore size distribution of cylindrical pores of $\sim$6.6 nm was observed. When compared to the parent material SBA-15, a significant decrease in surface area from 760 to $\sim$465 m^2 g^{-1}

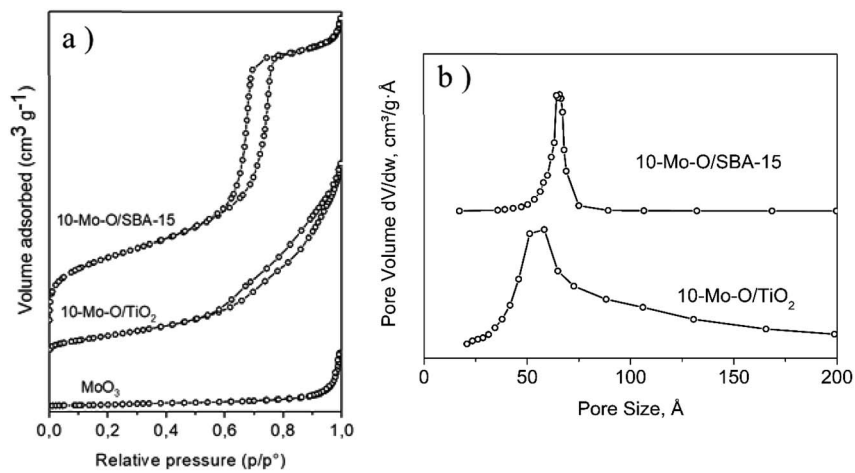

Fig. 2 (a) N_2 adsorption–desorption isotherms and (b) pore size distribution of 10-Mo-O/SBA-15 and 10-Mo-O/TiO_2.

Table 1 Textural and reducibility properties of the bulk and supported Mo-based materials

Sample	α-MoO_3[a] (wt%)	S_{BET}[b] ($m^2\ g^{-1}$)	S_{μ}[c] ($m^2\ g^{-1}$)	V_p[d] ($cm^3\ g^{-1}$)	D_p[e] (nm)	Mean particle size[f] (nm)
α-MoO_3	—	4	—	—	—	NA
SBA-15	—	760	131	1.1	6.5	NA
10-Mo-O/SBA-15	10.8	465	68	0.82	6.6	1.3 ± 0.3
TiO_2	—	135	3.8	0.44	12.0	NA
10-Mo-O/TiO_2	13.2	115	1	0.27	9.7	1.7 ± 0.7

[a] α-MoO_3 content in the calcined samples measured by ICP-OES. [b] BET surface area. [c] Microporous surface area. [d] Total pore volume. [e] BJH mean pore size. [f] Mean particle size of MoN_x estimated from HAADF-STEM analysis of a sample of 25 particles.

was observed, which was accompanied by a parallel decrease in pore volume. This is in accordance with partial filling of the mesopores by the molybdenum oxide phase. However, both SBA-15 and 10-Mo-O/SBA-15 display similar pore size distribution, indicating the formation of discrete molybdenum oxide nanoparticles in the pores of SBA-15. 10-Mo-O/TiO_2 exhibited a type IV isotherm with less marked hysteresis. The accessible surface area of 10-Mo-O/TiO_2 was found to be $\sim$115 $m^2\ g^{-1}$.

3.1.3 TEM-EDS studies. Following ammonia synthesis, the morphology of 10-Mo-N/SBA-15 and 10-Mo-N/TiO_2 was studied by means of HAADF-STEM analysis coupled with EDS mapping to investigate the local distribution of molybdenum. A selection of high resolution HAADF images of 10-Mo-N/SBA-15 and 10-Mo-N/TiO_2 is presented in Fig. 3 and S1.†

As observed in Fig. S1a,† the characteristic hexagonal array of SBA-15 with the typical 2D periodic hexagonal structure was maintained in 10-Mo-N/SBA-15 following the ammonia synthesis reaction. Furthermore, complementary EDS analysis confirms the high dispersion of molybdenum nitride species within the 2D-channels of SBA-15. In fact, the average particle size of molybdenum nitride

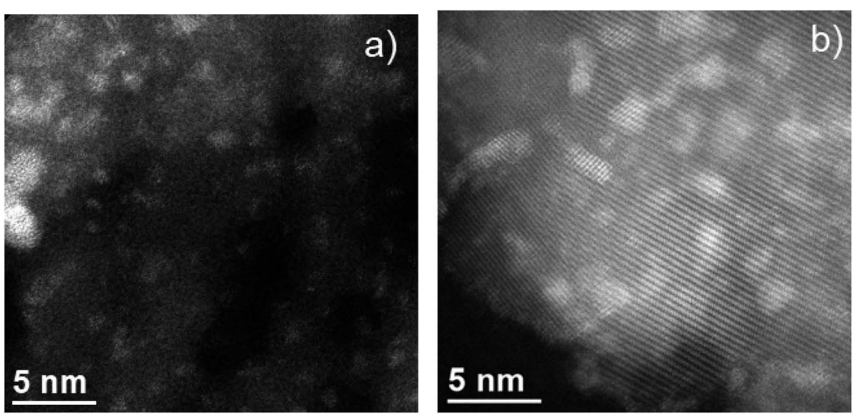

Fig. 3 Representative lower magnification HAADF images for (a) 10-Mo-N/SBA-15 and (b) 10-Mo-N/TiO_2.

was found to be 1.3 ± 0.3 nm (sample of 25 particles). In a similar manner, HAADF-STEM analysis revealed a high dispersion of molybdenum nitride species in the 10-Mo-N/TiO_2 catalyst (Fig. S1 (b–d)†). Furthermore, the particle size of molybdenum species was slightly larger than that observed in 10-Mo-N/SBA-15, which was estimated to be 1.7 ± 0.7 nm. In both 10-Mo-N/TiO_2 and 10-Mo-N/SBA-15 catalysts, STEM-EDX analysis confirmed the formation of small nanoparticles and the homogeneous distribution of molybdenum species within the support. Unfortunately, due to the small particle size, the low N concentration, and the low N K peak energy it was not possible to detect unambiguously the formation of MoN_x species.

3.2 Electronic properties of supported Mo samples: XPS and EPR studies

3.2.1 XPS studies. XPS analysis was performed for 10-Mo-O/SBA-15 and 10-Mo-O/TiO_2 on calcined materials. The active form of the catalysts was also studied by means of XPS by directly pre-treating the materials in the XPS environmental chamber at 700 °C for 2 h under a 60 mL min^{-1} flow of 75 vol% H_2/N_2. The results are presented in Fig. 4 and S2, and Tables 2 and S1–S3.†

3.2.2 Evolution of Mo oxidation states. To establish a basis for comparison, unsupported α-MoO_3 and β-Mo_2N were also investigated by XPS. As expected, in α-MoO_3, the predominant molybdenum species are Mo^{6+} (Table 2).[36,37] Upon pre-treatment, the Mo 3d XPS profile shifted to lower binding energy. The spectral decomposition of the Mo 3d region was composed predominantly of two oxidation states that can be ascribed to Mo^{4+} and Mo–N (Table 2).

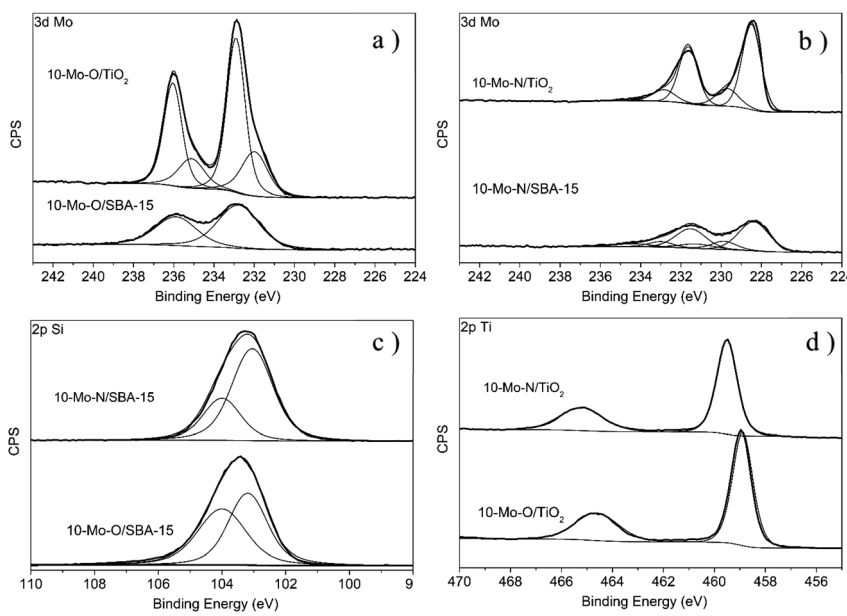

Fig. 4 XPS spectra recorded for the calcined materials (10-Mo-O/SBA-15 and 10-Mo-O/TiO_2) and after nitridation under reaction conditions at 700 °C for 2 h in the environmental XPS chamber. (a) Mo 3d region: 10-Mo-O/SBA-15 and 10-Mo-O/TiO_2, (b) Mo 3d region: 10-Mo-N/TiO_2 and 10-Mo-N/SBA-15, (c) Si 2p region: 10-Mo-O/SBA-15 and 10-Mo-N/SBA-15 and (d) Ti 2p region: 10-Mo-O/TiO_2 and 10-Mo-N/TiO_2.

Table 2 Positions of the 3d Mo peaks of unsupported and supported Mo based catalysts under different reaction conditions

	Mo peaks								Surface composition			
	Mo(VI)		Mo(V)		Mo(IV)		Mo–N					
	$3d_{5/2}$	$3d_{3/2}$	$3d_{5/2}$	$3d_{3/2}$	$3d_{5/2}$	$3d_{3/2}$	$3d_{5/2}$	$3d_{3/2}$	Mo(VI) (%)	Mo(V) (%)	Mo(IV) (%)	Mo–N (%)
Mo-O/TiO_2	232.91	236.05	231.99	235.13	—	—	—	—	70.93	29.07	—	—
Mo-N/TiO_2[a]	—	—	231.00	234.14	229.7	232.84	228.49	231.63	—	0.73	21.89	77.39
Mo-O/SBA-15	232.8	235.9	—	—	—	—	—	—	100	—	—	—
Mo-N/SBA-15[a]	232.26	235.40	—	—	230.05	233.19	228.36	231.50	12.76	—	20.84	66.40
β-Mo_2N	—	—	—	—	229.50	232.65	228.78	231.92	—	—	36.34	63.65
α-MoO_3	233.19	236.29	—	—	—	—	—	—	100	—	—	—

[a] Catalyst subject to pre-treatment under reaction conditions at 700 °C for 2 h in the environmental XPS chamber before analysis.

The evolution of the surface chemical composition of the supported Mo catalysts has also been studied and compared to that of the unsupported materials. For instance, 10-Mo-O/SBA-15 showed a similar Mo 3d XPS profile to the unsupported α-MoO_3 phase with only two major spectral lines corresponding to the Mo $3d_{5/2}$ and Mo $3d_{3/2}$ spin–orbit components at 232.8 eV and 235.9 eV, which were attributed to the formal Mo^{6+} oxidation state, with a small shift when compared to the reference material (Fig. 4). Interestingly, in the case of 10-Mo-O/TiO_2, the spectral decomposition of the high-resolution Mo 3d region revealed the presence of both Mo^{6+} and Mo^{5+} species.[36] The distribution of Mo oxide species was determined to be ~70.93 at% and ~29.07 at% for Mo^{6+} and Mo^{5+} respectively (Table 2). The stabilization of a large fraction of Mo^{5+} in 10-Mo-O/TiO_2 might be related to the strong interaction between Mo species and TiO_2. The isomorphic substitution of Ti^{4+} species by Mo^{5+} has been reported in the literature as both species possess very similar ionic radii (Ti^{4+}: 0.605 Å, and Mo^{5+}: 0.61 Å).[38]

Following the pre-treatment step, a noticeable change in the Mo 3d XPS profile can be observed for both 10-Mo-N/SBA-15 and 10-Mo-N/TiO_2 characterized by an important shift to lower binding energies. In 10-Mo-N/SBA-15, the high-resolution Mo 3d XPS profile can be deconvoluted into several peaks. The peaks at 228.36 eV and 231.50 eV are correlated with the $3d_{5/2}$ and $3d_{3/2}$ states of Mo–N species[39] which are the main Mo species (66.40 at%; Table 2), suggesting that the nitridation of Mo species is not complete. Additional peaks at 232.26 eV and 235.40 eV that can be correlated to the presence of Mo^{6+} and peaks at 230.05 eV and 233.19 eV that can be correlated with Mo^{4+} have also been observed. In the case of the 10-Mo-N/TiO_2 catalyst, the deconvolution of the high-resolution Mo 3d XPS profile revealed a chemical composition dominated by Mo–N (~77.39 at%) and Mo^{4+} (~21.89 at%). In summary, following the activation process, in all catalysts, a large fraction of Mo species were present as molybdenum nitrides (>60 at%).

Further details on the degree of molybdenum nitridation can be extracted from the high-resolution Mo 3p spectra in which N 1s can also be observed (Fig. S2†). Due to the overlapping of N 1s with Mo $3p_{3/2}$ peaks, it is difficult to deconvolute these peaks in a very detailed manner. Nevertheless, useful information can still be deduced. When compared to the oxides, the high-resolution Mo 3p XPS profiles of β-Mo_2N, 10-Mo-N/SBA-15 and 10-Mo-N/TiO_2 were all shifted to lower binding energies which can be associated with the nitridation of Mo species. For 10-Mo-N/SBA-15, peaks related to N 1s and Mo $3p_{3/2}$ were significantly overlapped. Nevertheless, in the case of 10-Mo-N/TiO_2 an intense and well resolved peak at 398.00 eV, which is attributed in the literature to N 1s in MoN and bulk Mo_2N (397.8 eV), was observed.[40] The same peak was observed in our unsupported β-Mo_2N materials but with less intensity. An additional, very weak in intensity peak only observed in the case of 10-Mo-N/TiO_2 at 400.8 eV was also detected. This might be attributed to N–H or adsorbed NH_3 as its binding energy is very close to the value reported for adsorbed NH_3.[41] NH_3 species are formed during the activation under a $N_2:H_2$ atmosphere in conditions favourable for ammonia synthesis.

3.2.3 Evolution of the support surface redox properties. The evolution of the support surface characteristics has also been studied. For SBA-15, no shift in binding energy was reported which is in agreement with the non-redox nature of the support (Fig. 4c). Although, following the pre-treatment step, changes in the intensity of the two components of the Si 2p peak, namely Si–O–Si and Si–O–H

(104 and 103.1 ± 0.05 eV respectively), are detected. The inversion of intensity detected is more related to modification of the concentration of the external functional groups when subject to a reducing atmosphere under reduction conditions (Fig. 4c and Table S1†). For the TiO_2 support more visible changes are observed after the pre-treatment. In 10-Mo-O/TiO_2 (Fig. 4d and Table S2†), the binding energies of Ti $2p_{3/2}$ and Ti $2p_{1/2}$ were 458.89 and 464.61 eV, at slightly higher binding energies when compared with values reported for Ti^{4+} in the undoped TiO_2 anatase phase (Ti $2p_{3/2}$: 458.59 eV and Ti $2p_{1/2}$: 464.31 eV).[42] This slight shift to higher binding energy (~0.3 eV) has been attributed to charge redistribution between Mo and Ti species.[38,43] However, after the activation step, a further shift to higher binding energies of Ti^{4+} is observed (Ti $2p_{3/2}$: 459.51 eV and Ti $2p_{1/2}$: 465.23 eV). In our nitridation conditions, the formation of titanium oxynitrides/nitrides or reduction of Ti^{4+} to Ti^{3+} can be safely ruled out as both outcomes are accompanied by a marked shift in Ti 2p positions to lower binding energy.[44]

3.2.4 Support surface composition. XPS analysis also allows us to assess the effect of the nature of the support and the pre-treatment step in affecting the surface composition (Table S3†). First of all, the Mo atomic surface concentration was found to be higher in 10-Mo-O/TiO_2 (12.5 at%) than 10-Mo-O/SBA-15 (4.3 at %). This might be related to Mo being impregnated within the pores and channels of SBA-15 rather than the external surface. However, when subject to the activation step, the concentration of Mo in the surface is only slightly modified in 10-Mo-N/SBA-15 (3.57 at%), whereas in the case of 10-Mo-N/TiO_2 a more pronounced decrease in surface Mo, of ~21%, is observed suggesting a strong interaction between Mo and Ti species.

3.2.5 EPR studies. While molybdenum displays a range of oxidation states, only Mo^{5+} is paramagnetic and can yield an EPR signal. As such, EPR is valuable in studying the process of nitridation of Mo species; the results are shown in Fig. 5.

The EPR spectrum recorded for 10-Mo-O/TiO_2, prior to the pre-treatment step, displays a weak isotropic signal centred at $g = 1.95$, indicating the presence of Mo^{5+} species. The presence of Mo^{5+} was also confirmed by XPS analysis (Table 2 and Fig. 4a). Additionally, a weak signal is observed, around $g = 2$, revealing the presence of oxygen vacancies.[45] During the activation process, under *in situ* H_2/N_2, a sharp increase in Mo^{5+} content is detected, reaching a maximum after 15 minutes of reaction at 700 °C. Thereafter, the concentration of Mo^{5+} decreases and stabilizes after a period of 20 minutes (Fig. 5c). The spectrum displayed in Fig. 5a shows the EPR signal recorded at 293 K at the end of the kinetic evolution. The spectrum displays a weak anisotropy of the g factor with $g_{x,y} = 1.97$ and $g_z = 1.93$. In contrast, the evolution of the oxygen vacancy concentration followed the reverse of that of Mo^{5+}. First, the concentration of oxygen vacancies decreased until reaching a minimum at 15 min of reaction and slightly increased afterwards to remain stable after 20 min. For 10-Mo-O/SBA-15 only a weak signal of Mo^{5+} and oxygen vacancies is detected. During the pre-treatment step no changes are observed in the concentration of both species. For the 10-Mo-O/SBA-15 catalyst, as EPR measures only Mo(v) content, the XPS results may reveal fast electron exchange between oxygen vacancies and Mo that can contribute to overestimating the Mo(v) content.

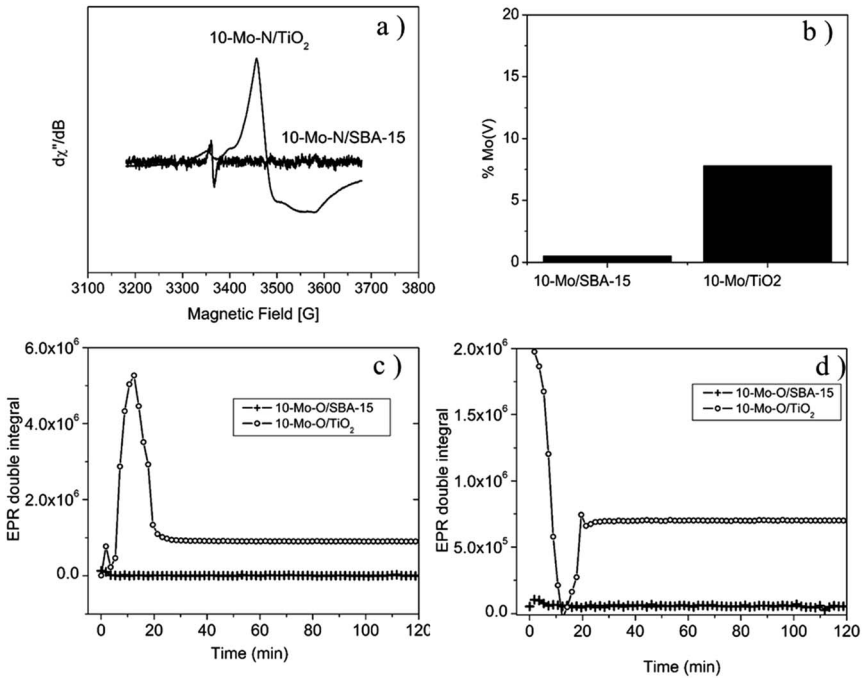

Fig. 5 EPR results: (a) EPR spectra after reaction, (b) fraction of Mo^{5+} after pre-treatment, (c) kinetic evolution of Mo^{5+} species at 700 °C under hydrogen, and (d) kinetic evolution of O^{n-} species at 700 °C under H_2/N_2.

Both XPS and EPR spectroscopy proved to be effective in measuring redox changes of Mo-based catalysts during the pre-treatment step. The activation process seems to proceed differently depending on the nature of the support. It seems that the nitridation process of Mo species, when supported on SBA-15, occurs *via* the direct reduction of Mo species to Mo^{4+}. However, during the nitridation process of Mo species in the case of TiO_2, the formation of Mo^{5+} was detected, hinting that the process might proceed *via* the formation of an $H_xMo^{5+}{}_xMo^{6+}{}_{1-x}O_3$ species.[46]

3.3 H_2-temperature programmed reduction (H_2-TPR)

Fig. 6 depicts the results of molybdenum oxide reducibility when supported on SBA-15 and TiO_2. The results were compared with the unsupported α-MoO_3 phase.

The reduction profile of the unsupported α-MoO_3 phase was characterized by two main reduction peaks at 770 and 980 °C and a smaller shoulder at around 800 °C. However, the reduction process was not complete at a temperature as high as 980 °C. The profile agrees well with the literature with a first reduction step of α-MoO_3 to MoO_2, characterized by a sharp reduction peak, followed by the reduction of MoO_2 to the metallic form at high temperature.[47] The shoulder at around 800 °C was attributed in the literature to the formation of intermediate phases, such as Mo_4O_{11}, during the reduction process.[47]

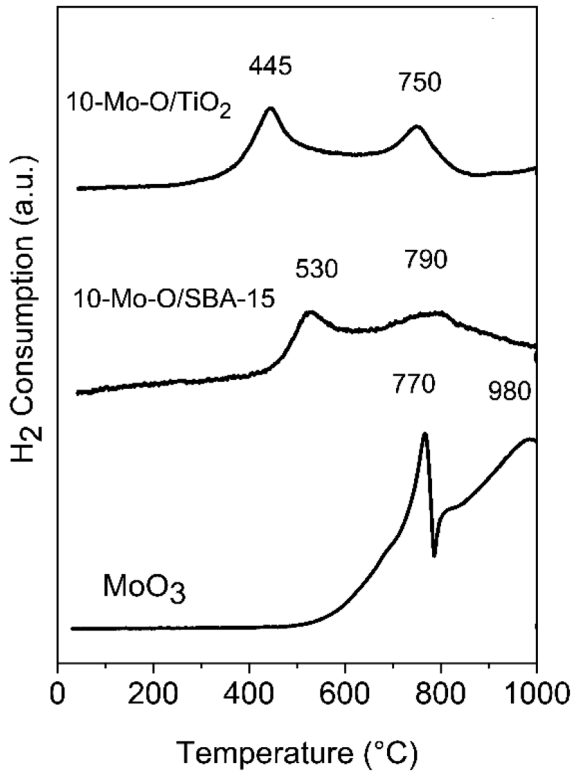

Fig. 6 H_2-TPR profiles of α-MoO_3, 10-Mo-O/SBA15 and 10-Mo-O/TiO_2.

The reducibility of Mo oxide species was strongly affected by their dispersion in SBA-15 and TiO_2. In both 10-Mo-O/SBA-15 and 10-Mo-O/TiO_2, the reduction profile shifted to lower temperature. Depending on the nature of the support, the first reduction step started at a temperature as low as 445 °C for 10-Mo-O/TiO_2, and a higher reduction temperature of ~530 °C for 10-Mo-O/SBA-15 was observed. These small differences between SBA-15 and TiO_2 might be related to the differences, observed by XPS, in the surface composition of the samples (Table 2). The second reduction step has also shifted to lower temperature with slight differences observed between SBA-15 and TiO_2. In summary, the reactivity of molybdenum oxides increased significantly upon their dispersion into high surface area supports, confirming the high reactivity of small nanoparticles towards hydrogen when compared to unsupported molybdenum species.

3.4 H_2-temperature programmed desorption (H_2-TPD)

The effect of the support on the adsorption–desorption properties of 10-Mo-N/TiO_2 and 10-Mo-N/SBA-15 was studied by means of H_2-TPD. The results are shown in Fig. 7 and Table S5.† For 10-Mo-N/TiO_2, the desorption profile was characterised by two desorption peaks, the first one appearing from 100 °C to 350 °C and the second desorption peak appearing from 350 °C to 600 °C. In both desorption events, only a small quantity of hydrogen is observed. However, in 10-Mo-N/SBA-

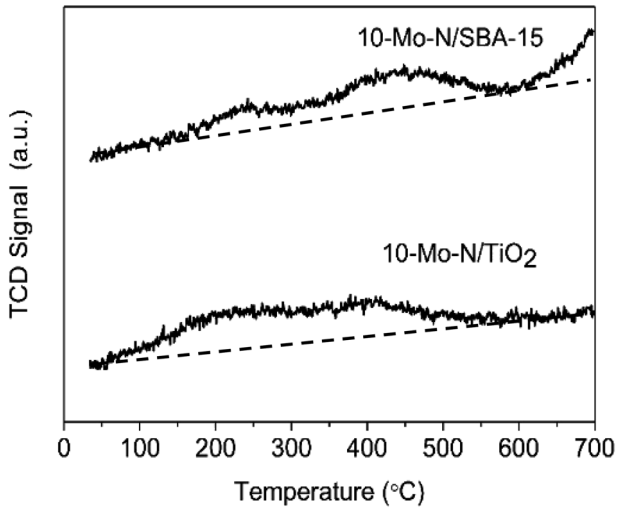

Fig. 7 H_2-TPD profiles of 10-Mo-N/SBA15 and 10-Mo-N/TiO_2.

15, the quantities of hydrogen desorbed were more pronounced, especially for the second peak of hydrogen desorption. Furthermore, H_2-desorption continued at higher temperature (>600 °C) which was not the case in the 10-Mo-N/TiO_2 sample. These results indicate a strong effect of the nature of the support in tuning molybdenum hydrogen adsorption–desorption properties. The drop in H_2-desorption capacity at high temperature might be indicative of SMSI behaviour affecting the ability of Mo species to activate hydrogen.

3.5 Catalytic activity in model reactions: ammonia synthesis and ammonia decomposition

The performance of 10-Mo-N/SBA-15 and 10-Mo-N/TiO_2 in ammonia synthesis and the opposite reaction (ammonia decomposition) was studied. The results are summarized in Fig. 8 and Table 3.

The catalytic activity of the 10-Mo-N/SBA-15 and 10-Mo-N/TiO_2 catalysts was studied in ammonia synthesis and compared against the unsupported β-Mo_2N (Fig. 8a, Table 3). 10-Mo-N/SBA-15 exhibits catalytic activity that is comparable to that of the reference material despite large differences in Mo loading (10-Mo-N/SBA-15: 84.6 μmol g_{cat}^{-1} $h^{-1}$and β-Mo_2N: 76 μmol g_{cat}^{-1} h^{-1} for the initial rate (30–60 min)). When normalised against the active phase loading, a rate of 1208 μmol $g_{active\ phase}^{-1}$ h^{-1} is obtained over the 10-Mo-N/SBA-15 catalyst. After a period of stabilisation, the catalyst didn't show any sign of deactivation over time, demonstrating its stability in the H_2 : N_2 stream. Surprisingly, 10-Mo-N/TiO_2 displayed a very poor catalytic activity and deactivated very quickly. The limited catalytic activity of 10-Mo-N/TiO_2 despite its enhanced textural and structural properties demonstrated a marked influence of the nature of the support in altering the ability of Mo to catalyse the ammonia synthesis reaction.

To confirm whether TiO_2 will affect in a similar manner the activity of Mo species in the reverse reaction, the activity of 10-Mo-N/SBA-15 and 10-Mo-N/TiO_2 has also been studied in ammonia decomposition. The catalytic activity was

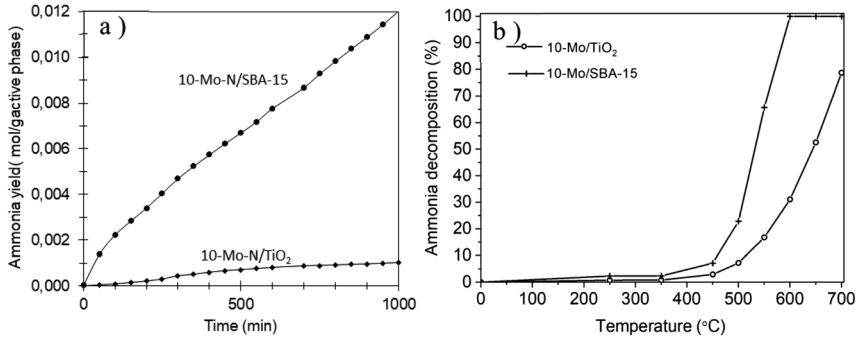

Fig. 8 (a) Cumulative ammonia yield obtained for 10-Mo-N/SBA-15 and 10-Mo-N/TiO_2. Reaction performed under 60 mL min^{-1} flow rate of 75 vol% H_2/N_2 at 400 °C and ambient pressure. (b) Ammonia decomposition conducted under 15% NH_3 in Ar at different temperatures and atmospheric pressure.

measured at temperatures ranging between 50 °C and 700 °C and the results are presented in Fig. 8b and Table 3. Unlike in ammonia synthesis, both catalysts, 10-Mo-N/SBA-15 and 10-Mo-N/TiO_2, are active in ammonia decomposition. However, differences in the catalytic activity are observed especially at high temperature. At low temperature, 10% NH_3 conversion is achieved at 460 °C on 10-Mo-N/SBA-15 while the same conversion value is achieved at slightly higher temperature (~510 °C) in the case of 10-Mo-N/TiO_2. The activation energy is slightly lower in the case of 10-Mo-N/SBA-15 (71 kJ mol^{-1}) when compared to 10-Mo-N/TiO_2 (78 kJ mol^{-1}). At higher temperature, complete conversion of NH_3 was achieved at 600 °C on 10-Mo-N/SBA-15, while on the 10-Mo-N/TiO_2 catalyst complete conversion wasn't attained even at a temperature as high as 700 °C. In summary, while supporting Mo over titania didn't turn off the catalytic activity in ammonia decomposition, lower conversions are clearly obtained compared to 10-Mo-N/SBA-15.

4 Discussion

The catalytic properties of the supported Mo nitrides in both ammonia synthesis and ammonia decomposition were found to be markedly affected by the nature of the support (TiO_2 or SBA-15). Depending on the catalytic reaction, disparities in how the support affects the catalytic activity of Mo species were found. When ammonia synthesis was studied, Mo nitride supported on SBA-15 was found to be active and stable over time. But when supported on TiO_2 a very limited catalytic activity was observed and the catalyst deactivated quite rapidly. This indicates that the properties of Mo active species varied with the nature of the support. In ammonia decomposition, the effect of the support was not as "radical" as observed in ammonia synthesis. While 10-Mo-N/SBA-15 was far more active than 10-Mo-N/TiO_2, the activity of the latter didn't turn-off completely.

In the current study, the active phase, MoN_x, was prepared by nitridation under a 75 vol% H_2/N_2 (BOC, 99.98%) gas mixture at a total gas flow of 60 mL min^{-1} for 2 h at 700 °C. To investigate the differences between the catalysts, the textural and structural properties have been studied. Both catalysts displayed

Table 3 Summary of the catalytic activity of 10-Mo-N/SBA-15 and 10-Mo-N/TiO_2

	Ammonia synthesis reaction[a]				Ammonia decomposition[b]		
	Initial rate (μmol $g_{catalyst}^{-1}$ h^{-1})	Initial rate (μmol $g_{active\ phase}^{-1}$ h^{-1})	Steady state rate (μmol $g_{catalyst}^{-1}$ h^{-1})	N[c] (wt%)	T_{10}	T_{100}	E_a (kJ mol^{-1})
β-Mo_2N	76	76	77	5.9	—	—	—
10-Mo-N/SBA-15	84.6	1208	50.74	1.1	460	585	71
10-Mo-N/TiO_2	ND[d]	ND	ND	1.2	510	—	78

[a] Ammonia synthesis under a 60 mL min^{-1} flow of 75% H_2 in N_2 (BOC, 99.98%) at 400 °C and atmospheric pressure. [b] Ammonia decomposition conducted under 15% NH_3 in Ar at different temperatures and atmospheric pressure. [c] Nitrogen content measured by CHNS analysis of post-reaction samples. [d] ND: not detected. T_{10}: temperature at which 10% NH_3 conversion is achieved. T_{100}: temperature at which 100% NH_3 conversion is achieved.

high accessible surface area (10-Mo-O/SBA-15: 465 $m^2\ g^{-1}$ and 10-Mo-O/TiO_2: 194 $m^2\ g^{-1}$). Furthermore, in both catalysts, no PXRD peaks related to Mo oxide or nitride phases are observed in the wide-angle domain, confirming the high dispersion of the active sites. The formation of small Mo nanoparticles was also confirmed by HAADF-STEM analysis. The particle size of molybdenum species was found to be reasonably similar in 10-Mo-N/SBA-15 (1.3 ± 0.3 nm) and in 10-Mo-N/TiO_2 (1.7 ± 0.7 nm). Thus, in both catalysts, after the activation step, small size nanoparticles were formed. Hence the effect of particle size in influencing the catalytic activity can be considered minimal.

The influence of the support on the surface composition was investigated by means of XPS spectroscopy and compared against a reference material. Before the activation step, a difference in Mo species detected by XPS was already observed. In both α-MoO_3 and Mo-O/SBA-15, the predominant Mo species was Mo^{6+} (Table 2, Fig. 4). However, ~29.07 at% of Mo species in 10-Mo-O/TiO_2 was found to be composed of Mo^{5+} with possible substitution of Ti^{4+} species by Mo^{5+}.[38] Furthermore, in 10-Mo-O/TiO_2, the binding energies of Ti $2p_{3/2}$ and Ti $2p_{1/2}$ were found at 458.89 and 464.61 eV, which are slightly higher when compared with values reported in the literature which further confirms the strong interaction of Mo species with titanium species.[42,43] Upon nitridation, a range of oxidation states have been detected. In both catalysts, a high proportion of Mo species were found to be in the nitride form (>60 at%). However, after the activation step, only Mo^{4+} species and MoN_x species are detected in 10-Mo-N/TiO_2 while in 10-Mo-N/SBA-15, in addition to Mo^{4+} species and MoN_x a fraction of Mo^{6+} was still present in the catalyst after the activation step, indicating an incomplete nitridation process. Despite these differences, the percentage of Mo nitrides in both systems seems to be rather close (10-Mo-N/TiO_2: 77.39 at% and 10-Mo-N/SBA-15: 66.40 at%). The degree of Mo species nitridation was also observed from the high-resolution Mo 3p spectra in which N 1s can also be observed. Only in the case of 10-Mo-N/TiO_2 an intense and well resolved peak at 398.00 eV, which is attributed in the literature to N 1s in bulk MoN and Mo_2N (397.8 eV), is observed which may reflect a different Mo/N ratio in the catalyst. An additional, very weak in intensity peak only observed in the case of 10-Mo-N/TiO_2 at 400.8 eV is also detected which was attributed to N–H or adsorbed NH_3.

To gain insight in the nitridation process of supported Mo oxide species, EPR and H_2-TPR have been conducted. When compared to the α-MoO_3 phase, the reduction process started earlier in the supported catalysts with the first reduction step starting at a temperature as low as 445 °C for 10-Mo-O/TiO_2 and a slightly higher reduction temperature of ~530 °C for 10-Mo-O/SBA-15. These differences might be related to the difference in Mo oxide species present on the surface as evidenced by XPS. Furthermore, the activation process was studied by EPR under a 75 vol% H_2/N_2 (BOC, 99.98%) gas mixture mimicking the activation step. Fundamental differences were observed between the 10-Mo-O/SBA-15 and 10-Mo-O/TiO_2 materials. In the case of Mo supported on TiO_2, the nitridation/reduction process occurs first *via* the formation of Mo^{5+} species as detected by EPR which reached a maximum concentration after 12 min reaction before the concentration started decreasing. Although only a very small fraction is detected by XPS, EPR shows that a fraction of Mo^{5+} (7.8%) is still present in the 10-Mo-O/TiO_2 catalyst directly after the activation step. The fast formation of Mo^{5+} might be indicative of a multistep reduction process with first intercalation of hydrogen into α-MoO_3 to

form first hydrogen molybdenum bronzes $H_xMo^{5+}{}_xMo^{6+}{}_{1-x}O_3$.[46] Hydrogen molybdenum bronzes are metastable phases that will decompose eventually to form MoO_2 and water.[48] In contrast, no Mo^{5+} was detected when Mo species were supported on SBA-15, indicating that the process is rather dominated by direct reduction of Mo^{6+} to Mo^{4+}. These differences might be related to different mechanisms by which Mo species are reduced/nitrided. In the literature, different mechanisms have been proposed including the formation of either molybdenum bronze ($H_xMo^{5+}{}_xMo^{6+}{}_{1-x}O_3$) and/or MoO_2 and Mo metallic intermediates before nitridation. Depending on the nitridation conditions (*i.e.* gas composition, space velocity and/or heating rate), the nitridation mechanism can be altered leading to the formation of either cubic γ-Mo_2N or tetragonal β-Mo_2N.[49,50] The formation of β-Mo_2N has been reported to follow a non-topotactic route *via* a multiple step reduction ($MoO_3 \rightarrow MoO_2 \rightarrow Mo \rightarrow MoN_x$).[51,52] While the formation of γ-Mo_2N has been reported to proceed through a topotactic route with the formation of hydrogen molybdenum bronze as an intermediate species before nitridation.[53] It's clear from our investigation that the mechanism of reduction/nitridation is strongly affected by the degree of interaction between Mo species and the support species. However, due to the formation of small nanoparticles in both SBA-15 and TiO_2, and the similar chemical composition of β-Mo_2N and γ-Mo_2N, it was rather difficult to unambiguously determine the nature of MoN_x species based on XRD and XPS results. As the activity of Mo_2N species in many catalytic reactions was found to vary depending on the crystallographic phase, it's tempting to explain the differences in the catalytic activity of 10-Mo-N/SBA-15 and 10-Mo-N/TiO_2 in ammonia synthesis by the formation of different Mo_2N allotropic forms. However, it is worth mentioning that no large differences in the catalytic activity have been found between bulk β-Mo_2N and γ-Mo_2N in ammonia synthesis and only the δ-MoN nitride phase was found to be poorly active in ammonia synthesis.[30] As such the identification of the catalytically active site and the origin of deactivation in Mo species supported on TiO_2 remains very challenging. In the literature, the performance of catalysts in the ammonia synthesis reaction has been correlated to nitrogen binding energy with the ideal surface displaying intermediate nitrogen binding energies. The adsorption properties of metal nitrides were found to be sensitive to chemical composition (surface *vs.* bulk), Mo oxidation states, $Mo^{\delta+}$/N ratio, and nitrogen-deficient site density.[52] To some extent, differences in H_2 adsorption–desorption capacities, at least at high temperature, were observed between 10-Mo-N/SBA-15 and 10-Mo-N/TiO_2. The surface composition after the activation step, and the reduction/nitridation process was found to be different depending on the nature of the support. Thus, the differences observed in the catalytic activity might be related to the differences observed in the surface composition and changes in the adsorption of ammonia synthesis reactants.

5 Conclusion

In the current study supported Mo nitride species on SBA-15 and TiO_2 were prepared by nitridation under a 75 vol% H_2/N_2 (BOC, 99.98%) gas mixture at a total gas flow of 60 mL min^{-1} for 2 h at 700 °C. The results of characterisation demonstrate the formation of small molybdenum nanoparticles in both 10-Mo-N/SBA-15 and 10-Mo-N/TiO_2 catalysts. Although both samples exhibited ameliorated structural properties when compared to the bulk material, β-Mo_2N, only 10-Mo-N/

SBA-15 was found to be active in ammonia synthesis (1208 μmol $g_{active\ phase}^{-1}\ h^{-1}$) while 10-Mo-N/$TiO_2$ only displayed a poor catalytic activity before completely deactivating over time. The catalysts were also studied for ammonia decomposition where 10-Mo-N/SBA-15 was found to be more active than 10-Mo-N/TiO_2. XPS analysis showed a strong interaction between Mo species and the TiO_2 support leading to differences in the Mo species reduction/nitridation process. EPR spectroscopy proved to be effective in determining the nitridation mechanism of Mo species. In the case of Mo supported on TiO_2, EPR showed that the reduction/nitridation process occurred *via* the formation of Mo^{5+} species which was not the case in Mo supported on SBA-15, suggesting the formation of different Mo nitride species. Upon nitridation, the distribution of Mo oxidation states was found to be different depending on the nature of the support. Furthermore, a weak XPS signal related to adsorbed NH_x species was detected in the 10-Mo-N/TiO_2 catalyst. It is also worth noting that the 10-Mo-N/SBA-15 hydrogen chemisorption capacity and desorption (during TPD) were superior to those of the 10-Mo-N/TiO_2 catalyst. The Mo species deactivation in ammonia synthesis when supported on TiO_2 probably originates from the strong interaction between Mo species and the support. This phenomenon resulted in the alteration of the Mo nitridation mechanism, leading to a catalyst with different surface composition, and probably different surface terminations, vacancy concentrations, *etc.* These results demonstrate that the catalytic activity of Mo nitride species can be tuned *via* modulation of the interaction between the active species and the support.

Conflicts of interest

There are no conflicts to declare.

Acknowledgements

The authors would like to thank Pardis Simon for XPS facilities and Anne-Marie Blanchenet for TEM facilities. Laassiri wishes to acknowledge the Foundation I-SITE ULNE/France for support through the grant ERC Generator and the program MOGPA. The French national research agency is acknowledged for support *via* the program Make Our Planet Great Again. Chevreul Institute (FR 2638), Ministère de l'Enseignement Supérieur, de la Recherche et de l'Innovation, Région Hauts de France and FEDER are acknowledged for supporting and funding partially this work.

References

1 A. N. Varakin, A. V. Mozhaev, A. A. Pimerzin and P. A. Nikulshin, *Appl. Catal., B*, 2018, **238**, 498.
2 H. Topsøe and B. S. Clausen, *Appl. Catal.*, 1986, **25**, 273.
3 M. M. H. Mondol, B. N. Bhadra and S. H. Jhung, *Appl. Catal., B*, 2021, **288**, 119988.
4 J. Zou, Y. Lin, S. Wu, Y. Zhong and C. Yang, *Adv. Funct. Mater.*, 2021, **31**, 2100442.
5 S. Singh, A. Modak, K. K. Pant, A. Sinhamahapatra and P. Biswas, *ACS Appl. Nano Mater.*, 2021, **4**, 8644.

6 Y. Kuwahara, T. Mihogi, K. Hamahara, K. Kusu, H. Kobayashi and H. Yamashita, *Chem. Sci.*, 2021, **12**, 9902.
7 N. Liu, L. Nie, N. Xue, H. Dong, L. Peng, X. Guo and W. Ding, *ChemCatChem*, 2010, **2**, 167.
8 N. Gavrilova, M. Myachina, V. Dyakonov, V. Nazarov and V. Skudin, *Nanomaterials*, 2020, **10**, 2053.
9 H. B. Wu, B. Y. Xia, L. Yu, X. Y. Yu and X. W. Lou, *Nat. Commun.*, 2015, **6**, 6512.
10 M. Nagae, T. Yoshio, Y. Takemoto and J. Takada, *J. Am. Ceram. Soc.*, 2001, **84**, 1175.
11 S. Wang, H. Ge, S. Sun, J. Zhang, F. Liu, X. Wen, X. Yu, L. Wang, Y. Zhang, H. Xu, J. C. Neuefeind, Z. Qin, C. Chen, C. Jin, Y. Li, D. He and Y. Zhao, *J. Am. Chem. Soc.*, 2015, **137**, 4815.
12 P. Xiao, M. A. Sk, L. Thia, X. Ge, R. J. Lim, J.-Y. Wang, K. H. Lim and X. Wang, *Energy Environ. Sci.*, 2014, **7**, 2624.
13 W. Cui, Q. Liu, Z. Xing, A. M. Asiri, K. A. Alamry and X. Sun, *Appl. Catal., B*, 2015, **164**, 144.
14 J. Lei, Y. Xie, A. Kutana, K. V. Bets and B. I. Yakobson, *J. Am. Chem. Soc.*, 2022, **144**, 7497.
15 S. Park, A. T. Garcia-Esparza, H. Abroshan, B. Abraham, J. Vinson, A. Gallo, D. Nordlund, J. Park, T. R. Kim, L. Vallez, R. Alonso-Mori, D. Sokaras and X. Zheng, *Adv. Sci.*, 2021, **8**, 2002768.
16 R. Kojima and K. Aika, *Appl. Catal., A*, 2001, **219**, 141.
17 A.-M. Alexander and J. S. Hargreaves, *Chem. Soc. Rev.*, 2010, **39**, 4388.
18 B. Y. Fang, C. F. Zhang, Z. L. Qi, C. Y. Li, J. Ni, X. Y. Wang, J. X. Lin, C. T. Au, B. Y. Lin and L. L. Jiang, *AIChE J.*, 2022, **68**, e17849.
19 B. Y. Fang, C. F. Zhang, J. H. Li, M. D. Yang, C. Y. Li, J. Ni, X. Y. Wang, J. X. Lin, B. Y. Lin and L. L. Jiang, *Chem. Commun.*, 2022, **58**, 7785.
20 L. Volpe and M. Boudart, *J. Phys. Chem.*, 1986, **90**, 4874.
21 C. J. H. Jacobsen, *Chem. Commun.*, 2000, 1057.
22 I. AlShibane, A. Daisley, J. S. J. Hargreaves, A. L. Hector, S. Laassiri, J. L. Rico and R. I. Smith, *ACS Sustainable Chem. Eng.*, 2017, **5**, 9214.
23 R. Kojima and K.-i. Aika, *Appl. Catal., A*, 2001, **218**, 121.
24 S. Al Sobhi, N. Bion, J. S. J. Hargreaves, A. L. Hector, S. Laassiri, W. Levason, A. W. Lodge, A. R. McFarlane and C. Ritter, *Mater. Res. Bull.*, 2019, **118**, 110519.
25 S. Yang, T. Zhang, Y. Y. Yang, B. X. Wang, J. Li, Z. T. Gong, Z. Y. Yao, W. G. Du, S. J. Liu and Z. L. Yu, *Appl. Catal., B*, 2022, **312**, 121404.
26 L. Li, W. K. Yu, W. B. Gong, H. Wang, C. L. Chiang, Y. P. Lin, J. Zhao, L. B. Zhang, J. M. Lee and G. F. Zou, *Appl. Catal., B*, 2023, **321**, 122038.
27 X.-W. Guo, S.-M. Chen, H.-J. Wang, Z.-M. Zhang, H. Lin, L. Song and T.-B. Lu, *J. Mater. Chem. A*, 2019, **7**, 19831.
28 S. Kim, Y. Park, J. Kim, T. P. Pabst and P. J. Chirik, *Nat. Synth.*, 2022, **1**, 297.
29 S. T. Oyama, *Catal. Today*, 1992, **15**, 179.
30 D. McKay, J. S. J. Hargreaves, J. L. Rico, J. L. Rivera and X. L. Sun, *J. Solid State Chem.*, 2008, **181**, 325.
31 K.-i. Aika and A. Ozaki, *J. Catal.*, 1969, **14**, 311.
32 B. Fang, M. Yang, C. Zhang, J. Li, C. Li, J. Ni, X. Wang, J. Lin, B. Lin and L. Jiang, *Chem. Eng. Sci.*, 2022, **259**, 117834.
33 Z. Luo, G. Zhao, H. Pan and W. Sun, *Adv. Energy Mater.*, 2022, **12**, 2201395.

34 H. Tang, Y. Su, B. Zhang, A. F. Lee, M. A. Isaacs, K. Wilson, L. Li, Y. Ren, J. Huang, M. Haruta, B. Qiao, X. Liu, C. Jin, D. Su, J. Wang and T. Zhang, *Sci. Adv.*, 2017, **3**, e1700231.
35 D. Zhao, J. Sun, Q. Li and G. D. Stucky, *Chem. Mater.*, 2000, **12**, 275.
36 J. Baltrusaitis, B. Mendoza-Sanchez, V. Fernandez, R. Veenstra, N. Dukstiene, A. Roberts and N. Fairley, *Appl. Surf. Sci.*, 2015, **326**, 151.
37 T. Weber, J. C. Muijsers, J. H. M. C. van Wolput, C. P. J. Verhagen and J. W. Niemantsverdriet, *J. Phys. Chem.*, 1996, **100**, 14144.
38 S. Esposito, N. Ditaranto, G. Dell'Agli, R. Nasi, P. Rivolo and B. Bonelli, *ACS Omega*, 2021, **6**, 5379.
39 L. Huo, X. Han, L. Zhang, B. Liu, R. Gao, B. Cao, W.-W. Wang, C.-J. Jia, K. Liu, J. Liu and J. Zhang, *Appl. Catal., B*, 2021, **294**, 120254.
40 M. Nagai, J. Takada and S. Omi, *J. Phys. Chem. B*, 1999, **103**, 10180.
41 R. J. J. Jansen and H. van Bekkum, *Carbon*, 1995, **33**, 1021.
42 M. C. Biesinger, L. W. M. Lau, A. R. Gerson and R. S. C. Smart, *Appl. Surf. Sci.*, 2010, **257**, 887.
43 D. Mittal, W. F. Chen, P. Koshy, H. K. Chen, I. Kabir, Y. Jiang, Z. Y. Liu and C. C. Sorrell, *SN Appl. Sci.*, 2019, **1**, 234.
44 J. Wang, D. N. Tafen, J. P. Lewis, Z. Hong, A. Manivannan, M. Zhi, M. Li and N. Wu, *J. Am. Chem. Soc.*, 2009, **131**, 12290.
45 C. Drouilly, J.-M. Krafft, F. Averseng, S. Casale, D. Bazer-Bachi, C. Chizallet, V. Lecocq, H. Vezin, H. Lauron-Pernot and G. Costentin, *J. Phys. Chem. C*, 2012, **116**, 21297.
46 A. Borgschulte, O. Sambalova, R. Delmelle, S. Jenatsch, R. Hany and F. Nüesch, *Sci. Rep.*, 2017, **7**, 40761.
47 T. Bhaskar, K. R. Reddy, C. P. Kumar, M. R. V. S. Murthy and K. V. R. Chary, *Appl. Catal., A*, 2001, **211**, 189.
48 J. J. Birtill and P. G. Dickens, *J. Solid State Chem.*, 1979, **29**, 367.
49 J.-G. Choi, R. L. Curl and L. T. Thompson, *J. Catal.*, 1994, **146**, 218.
50 S. Jujjuri, F. Cárdenas-Lizana and M. A. Keane, *J. Mater. Sci.*, 2014, **49**, 5406.
51 F. Cárdenas-Lizana, S. Gómez-Quero, N. Perret, L. Kiwi-Minsker and M. A. Keane, *Catal. Sci. Technol.*, 2011, **1**, 794.
52 N. Perret, D. Lamey, L. Kiwi-Minsker, F. Cárdenas-Lizana and M. A. Keane, *Catal. Sci. Technol.*, 2019, **9**, 1891.
53 F. Cárdenas-Lizana, D. Lamey, L. Kiwi-Minsker and M. A. Keane, *J. Mater. Sci.*, 2018, **53**, 6707.